INTERNATIONAL JOURNAL FOR NUMERICAL METHODS IN FLUIDS, VOL. 18, 887–914 (1994)

MULTIGRID SOLUTION OF COMPRESSIBLE TURBULENT FLOW ON UNSTRUCTURED MESHES USING A TWO-EQUATION MODEL

D. J. MAVRIPLIS

Institute for Computer Applications in Science and Engineering, NASA Langley Research Center, Hampton, VA 23665, U.S.A.

AND

L. MARTINELLI

Princeton University, Princeton, NJ, U.S.A.

SUMMARY

The steady state solution of the system of equations consisting of the full Navier–Stokes equations and two turbulence equations has been obtained using a multigrid strategy on unstructured meshes. The flow equations and turbulence equations are solved in a loosely coupled manner. The flow equations are advanced in time using a multistage Runge–Kutta time-stepping scheme with a stability-bound local time step, while the turbulence equations are advanced in a point-implicit scheme with a time step which guarantees stability and positivity. Low-Reynolds-number modifications to the original two-equation model are incorporated in a manner which results in well-behaved equations for arbitrarily small wall distances. A variety of aerodynamic flows are solved, initializing all quantitities with uniform freestream values. Rapid and uniform convergence rates for the flow and turbulence equations are observed.

KEY WORDS Unstructured Multigrid Turbulence Meshes

1. INTRODUCTION

The use of unstructured meshes has become more widespread in recent years owing to the ease with which complex geometries can be handled and the possibility of enhancing the solution accuracy and efficiency through adaptive meshing techniques. To date, most of the successes of unstructured mesh techniques have been in computing inviscid flows in two and three dimensions over arbitrary geometries. However, more recently, solutions of the Navier–Stokes equations on unstructured meshes have been reported.[1–5] The main obstacles to efficiently computing high-Reynolds-number flows on unstructured meshes are due to the required grid stretching and the turbulence model. For high-Reynolds-number flows over streamlined bodies, viscous effects are confined to thin boundary layer and wake regions, which can only be resolved efficiently using high-aspect-ratio elements. One approach[3,5] is to fit a thin local mesh of structured high-aspect-ratio quadrilaterals in the viscous regions and fill the remainder of the

CCC 0271–2091/94/100887–28

Received 3 April 1992
Revised 24 March 1993

domain with an unstructured mesh. The other approach consists of filling the entire domain with an unstructured mesh which contains highly stretched triangular elements in the viscous regions.[4] In this work the latter approach has been pursued in the interest of developing a more general method capable of dealing with a wider variety of flows, such as flows with confluent boundary layers or mixing wakes, and also to enable the straightforward implementation of adaptive meshing techniques throughout all regions of the flow field. The numerical scheme must therefore be formulated such that the accuracy and convergence are not seriously affected by the presence of highly stretched triangular elements.

The most commonly employed turbulence models for compressible flow calculations are of the algebraic mixing length type.[6] These models have been shown to produce good results for attached turbulent boundary layers and mildly separated flows using structured meshes, and have also been implemented for non-trivial geometries on unstructured meshes.[7] Although such models can be made inexpensive and computationally robust even in the context of unstructured meshes, they lack the generality required for dealing with completely arbitrary geometries, and their ability in predicting flows with multiple confluent shear layers and large amounts of separation is at best limited. Two-equation models, on the other hand, offer the possibility of dealing with the more complicated flows which are often associated with the complex geometries for which unstructured meshes are so well suited. In principle, the implementation of such models on unstructured meshes can be accomplished in a straightforward fashion simply by discretizing and integrating the turbulence equations in a manner analogous to that employed for the mean flow equations. However, field equation turbulence models have often proved to be extremely difficult to integrate to steady state, exhibiting stiff or unstable numerical behaviour in regions very close to the wall as well as in the far field. The use of multigrid to solve the turbulence equations has recently been reported by several authors[8,9] using an Ni-type scheme on structured meshes. In this work, a multigrid strategy which has previously been developed for the Euler and Navier–Stokes equations on unstructured meshes[4,10] is extended to solve the two turbulence equations as well.

2. GOVERNING EQUATIONS

The governing equations are obtained by Favre averaging the Navier–Stokes equations and modelling the Reynolds stress and heat flux terms by the Boussinesq assumption. In conservative form these equations are written as

$$\frac{\partial w}{\partial t} + \frac{\partial f_c}{\partial x} + \frac{\partial g_c}{\partial y} = \frac{\partial f_v}{\partial x} + \frac{\partial g_v}{\partial y}, \tag{1}$$

where w is the solution vector and f_c and g_c are the Cartesian components of the convective fluxes:

$$w = \begin{bmatrix} \rho \\ \rho u \\ \rho v \\ \rho E \end{bmatrix}, \qquad f_c = \begin{bmatrix} \rho u \\ \rho u^2 + p \\ \rho uv \\ \rho uE + up \end{bmatrix}, \qquad g_c = \begin{bmatrix} \rho v \\ \rho vu \\ \rho v^2 + p \\ \rho vE + vp \end{bmatrix}. \tag{2}$$

In the above equations ρ represents the fluid density, u and v are the x- and y-components of

the fluid velocity respectively, E is the total energy and p is the pressure, which can be calculated from the equation of state of a perfect gas:

$$p = (\gamma - 1)\rho\left(E - \frac{u^2 + v^2}{2}\right). \tag{3}$$

The viscous fluxes f_v and g_v are given by

$$f_v = \begin{bmatrix} 0 \\ \sigma_{xx} \\ \sigma_{xy} \\ u\sigma_{xx} + v\sigma_{xy} - q_x \end{bmatrix}, \qquad g_v = \begin{bmatrix} 0 \\ \sigma_{xy} \\ \sigma_{yy} \\ u\sigma_{yx} + v\sigma_{yy} - q_y \end{bmatrix}, \tag{4}$$

where σ represents the stress tensor and q the heat flux vector, which are given by

$$\sigma_{xx} = 2(\mu + \mu_t)u_x - \tfrac{2}{3}(\mu + \mu_t)(u_x + v_y) - \tfrac{2}{3}\rho k, \tag{5}$$

$$\sigma_{yy} = 2(\mu + \mu_t)v_y - \tfrac{2}{3}(\mu + \mu_t)(u_x + v_y) - \tfrac{2}{3}\rho k, \tag{6}$$

$$\sigma_{xy} = \sigma_{yx} = (\mu + \mu_t)(u_y + v_x), \tag{7}$$

$$q_x = -\frac{\gamma}{\gamma - 1}\left(\frac{\mu}{Pr} + \frac{\mu_t}{Pr_t}\right)\frac{\partial(p/\rho)}{\partial x}, \tag{8}$$

$$q_y = -\frac{\gamma}{\gamma - 1}\left(\frac{\mu}{Pr} + \frac{\mu_t}{Pr_t}\right)\frac{\partial(p/\rho)}{\partial y}. \tag{9}$$

Here μ represents the molecular viscosity and μ_t denotes the turbulent eddy viscosity, which must be computed by a suitable turbulence model. Pr is the laminar Prandtl number, which is taken as 0·7 for air, Pr_t is the turbulent Prandtl number, taken as 0·9, and γ is the ratio of specific heats of the fluid.

The high-Reynolds-number k–ε turbulence model originally described by Launder and Spalding[11] can similarly be written as

$$\frac{\partial w}{\partial t} + \frac{\partial f_c}{\partial x} + \frac{\partial g_c}{\partial y} = \frac{\partial f_v}{\partial x} + \frac{\partial g_v}{\partial y} + h, \tag{10}$$

where w, f_c and g_c are now given by

$$w = \begin{bmatrix} \rho k \\ \rho\varepsilon \end{bmatrix}, \qquad f_c = \begin{bmatrix} \rho uk \\ \rho u\varepsilon \end{bmatrix}, \qquad g_c = \begin{bmatrix} \rho vk \\ \rho v\varepsilon \end{bmatrix}. \tag{11}$$

The diffusive fluxes f_v and g_v are given by

$$f_v = \begin{bmatrix} \dfrac{\mu_t}{\sigma_k}\dfrac{\partial k}{\partial x} \\ \dfrac{\mu_t}{\sigma_\varepsilon}\dfrac{\partial \varepsilon}{\partial x} \end{bmatrix}, \qquad g_v = \begin{bmatrix} \dfrac{\mu_t}{\sigma_k}\dfrac{\partial k}{\partial y} \\ \dfrac{\mu_t}{\sigma_\varepsilon}\dfrac{\partial \varepsilon}{\partial y} \end{bmatrix} \tag{12}$$

and the source term h is given by

$$h = \begin{bmatrix} \mu_t P - \frac{2}{3}S\rho k - \rho\varepsilon \\ C_1 \frac{\varepsilon}{k}(\mu_t P - \frac{2}{3}S\rho k) - C_2 \rho \frac{\varepsilon^2}{k} \end{bmatrix}, \tag{13}$$

where the production term P and the term S in two dimensions are given by

$$P = \tfrac{4}{3}(u_x^2 + v_y^2 - u_x v_y) + (u_y + v_x)^2, \qquad S = u_x + v_y. \tag{14}$$

The eddy viscosity is calculated as

$$\mu_t = \rho C_\mu k^2/\varepsilon \tag{15}$$

and k also appears in the normal stresses in equation (5). The constants appearing in the above equations are given the standard values recommended in Reference 11, i.e.

$$C_\mu = 0{\cdot}09, \qquad \sigma_k = 1{\cdot}0, \qquad \sigma_\varepsilon = 1{\cdot}3, \qquad C_1 = 1{\cdot}44, \qquad C_2 = 1{\cdot}92. \tag{16}$$

These equations are coupled to the governing equations for the mean flow and exhibit a similar structure. Therefore a single system of equations which simultaneously governs the flow and turbulence quantities may be written as

$$\frac{\partial w}{\partial t} + \frac{\partial f_c}{\partial x} + \frac{\partial g_c}{\partial y} = \frac{\partial f_v}{\partial x} + \frac{\partial g_v}{\partial y} + h, \tag{17}$$

where the solution vector and the source term are now given by

$$w = \begin{bmatrix} \rho \\ \rho u \\ \rho v \\ \rho E \\ \rho k \\ \rho \varepsilon \end{bmatrix}, \qquad h = \begin{bmatrix} 0 \\ 0 \\ 0 \\ 0 \\ \mu_t P - \frac{2}{3}S\rho k - \rho\varepsilon \\ C_1 \frac{\varepsilon}{k}(\mu_t P - \frac{2}{3}S\rho k) - C_2 \rho \frac{\varepsilon^2}{k} \end{bmatrix} \tag{18}$$

and the flux definitions follow from equations (2), (4), (11) and (12).

The solution procedure consists of discretizing these equations in space on an unstructured mesh and then integrating the discretized equations in time until the steady state solution is obtained. The basic strategy pursued in this work involves the use of a finite element Galerkin discretization technique in conjunction with an unstructured multigrid integration technique to solve for the steady state. Although all six equations of the governing system are solved simultaneously in the multigrid strategy, the flow equations are only loosely coupled to the turbulence equations (through the value of μ_t) and we choose to employ somewhat different base grid solvers for the flow equations and the turbulence equations.

3. SPATIAL DISCRETIZATION

The equations governing the mean flow are discretized using a Galerkin finite element approach.[4] The flow variables are stored at the vertices of the triangles. The convective fluxes are computed

at the vertices of the triangles and assumed to vary linearly over the triangular elements. For the viscous terms the flow variables themselves are assumed to vary linearly over the triangular elements of the mesh and the required velocity gradients in the expression for the viscous stresses are thus computed at the centres of the triangular elements. Additional artificial dissipation terms are required to ensure the stability of the convective terms and these are constructed as a blend of a Laplacian and biharmonic operators in the conserved variables, designed to ensure second-order accuracy throughout the flow field, except in the vicinity of a shock where first-order accuracy is recovered. For the turbulence equations the diffusive terms are similarly discretized using a Galerkin finite element approach, assuming linear variations of the conserved variables over the triangular elements. The velocity gradients in the source terms are also constructed assuming linear elements. The convective terms, however, are constructed using first-order upwinding. Although only first-order-accurate, this approach is employed since it helps ensure stability and positivity of the conserved variables throughout the integration procedure, as will be shown. Furthermore, in regions where convection is small compared with the diffusion terms or the source terms, such as in the logarithmic law-of-the-wall region, the scheme reverts to second-order accuracy. In future work, however, a second-order-accurate implementation of the convective terms may be pursued.

4. INTEGRATION SCHEME

The discretized mean flow equations are integrated in time using an explicit five-stage Runge–Kutta time-stepping scheme in which the convective terms are evaluated at every stage and the dissipative terms are only evaluated at the first, third and fifth stages. This scheme, which has previously been described in References 4 and 12, has been particularly devised to ensure rapid damping of high-frequency errors and is thus well suited to drive the multigrid algorithm. Convergence is accelerated by the use of local time stepping and implicit residual averaging. In principle, the turbulence equations may be integrated in time using the same explicit scheme. However, the presence of source terms imposes a further time step restriction. If the flow equations and turbulence equations are integrated in a fully coupled manner, the minimum local time step from the flow and turbulence equations must be employed. In regions where the source terms dominate, this may lead to slow convergence. If, on the other hand, the flow equations and turbulence equations are integrated in an uncoupled explicit manner, the turbulence equations may significantly lag the flow equations and thus inhibit convergence to the steady state solution. In order to advance the turbulence quantities at the same rate as the flow equations, the source terms must be treated implicitly. However, rather than simply treat the source terms implicitly, the system of turbulence equations is integrated in a point-implicit manner. Thus we rewrite the discretized turbulence equations as

$$\Delta w_i/\Delta t = R(w_i) + H(w_i), \tag{19}$$

where $R(w_i)$ represents the discretized convective and diffusive terms, which depend on the values of w at i and at neighbouring nodes, and $H(w_i)$ represents the discretized source terms, which only depend on the values of w at i. The above equation is then linearized about the values at i, which, upon solving for Δw_i, yields

$$\Delta w_i = \left(\frac{1}{\Delta t} - \frac{\partial R}{\partial w} - \frac{\partial H}{\partial w}\right)^{-1} [R(w_i) + H(w_i)]. \tag{20}$$

The Runge–Kutta scheme described above is now replaced by a multistage implicit scheme in which the qth stage is given by

$$w^{(q)} = w^{(0)} + \left(\frac{1}{\alpha_q \Delta t} - \frac{\partial R}{\partial w} - \frac{\partial H}{\partial w}\right)^{-1} [R^{(q-1)}(w_i) + H^{(q-1)}(w_i)], \tag{21}$$

where the α_q denote the Runge–Kutta coefficients for the qth stage and Δt is the local time step. In this manner the high-frequency damping characteristics of the original scheme are approximated, while the time step restriction due to the source terms is alleviated. The precise value of the local time step Δt employed is one which guarantees stability as well as positivity of the turbulence quantities.

5. STABILITY AND POSITIVITY CONSIDERATIONS

One method to guarantee stability of the system is to ensure that the matrix to be inverted is diagonally dominant. This is not a necessary condition for stability, although it is sufficient. This can obviously be achieved by choosing Δt to be sufficiently small. However, the reason for employing a point-implicit approach now becomes apparent. Since the two turbulence equations are only coupled through their source terms, the matrix $\partial R/\partial w$ is diagonal. The contribution from the diffusive terms is strictly negative, as is that from the first-order upwinded convective terms. Hence these terms, when subtracted from the diagonal of the matrix to be inverted, increase the diagonal dominance and permit the use of a larger time step. The maximum value of Δt is found by equating each diagonal element to its corresponding off-diagonal element in the coefficient matrix. The actual value employed for the time step is taken as the minimum between the two values obtained by the diagonal dominance test and the value determined by local stability analysis for an explicit scheme in the absence of source terms.

Physically, k and ε represent quantities which must remain non-negative. Thus a further time step restriction is required to ensure positivity. For a simple 2×2 system this can easily be derived analytically. Thus we require that the new update to the turbulence variables be such that

$$w + \Delta w > \alpha w, \quad 0 < \alpha < 1,$$

or, when $\Delta w < 0$,

$$|\Delta w| < (1 - \alpha)w, \quad 0 < \alpha < 1. \tag{22}$$

Substituting into equation (20) and using Cramer's rule to evaluate the inverse of the 2×2 matrix, we obtain two quadratic inequalities for Δt, i.e. one for positivity of k and one for ε. The time step is then limited by the smallest positive root of the two quadratic equations.

6. MULTIGRID STRATEGY AND STEADY STATE CONSIDERATIONS FOR THE k–ε EQUATIONS

A multigrid strategy is employed to accelerate the solution of the system of mean flow and turbulence equations to steady state. In the context of unstructured meshes, multigrid may be applied by generating a sequence of non-nested coarse and fine meshes and transferring the variables, residuals and corrections back and forth between the various meshes using linear interpolation. The patterns for interpolating between non-nested unstructured meshes are determined in a preprocessing stage using an efficient search algorithm. The present multigrid

strategy has previously been described in detail for the Euler and Navier–Stokes equations[4,10] and thus will not be repeated here. In previous multigrid applications for turbulent flows using algebraic models on structured and unstructured meshes,[7,13] the eddy viscosities are only computed on the finest grid and interpolated to the coarser meshes. Since the eddy viscosity represents the main coupling between the flow equations and the turbulence equations, a similar approach has been adopted in the present context, thus ensuring a more accurate representation of this quantity on all grid levels. However, since the eddy viscosity is only computed on the finest grid, it is effectively held constant throughout an entire multgrid cycle and the source terms must be linearized accordingly. Making use of equations (11) and (13), the linearization of the source terms on all grids is therefore taken as

$$\frac{\partial H}{\partial w} = \begin{bmatrix} -\frac{2}{3}S & -1 \\ \dfrac{-C_1\mu_t P}{\rho}\dfrac{\varepsilon}{k^2} + C_2\dfrac{\varepsilon^2}{k^2} & C_1\left(\dfrac{\mu_t P}{\rho k} - \frac{2}{3}S\right) - 2C_2\dfrac{\varepsilon}{k} \end{bmatrix}. \tag{23}$$

At this point it is worth commenting on what types of errors may be expected to be handled efficiently by a multigrid strategy. Multigrid is an effective device for relieving the spatial stiffness associated with a set of discretized equations, which is achieved by time stepping on coarser grids. The turbulence equations contain spatial terms such as convection and diffusion, but the source terms are purely local terms. In fact, in the absence of convection and diffusion the equations become completely uncoupled in space and a properly formulated multigrid algorithm should yield vanishingly small corrections in such a case. Thus it is important for the base grid solver to efficiently eliminate errors associated with these terms. From another point of view, if a purely explicit scheme were employed, a time step restriction would arise from the convection, diffusion and source terms. While the first two restrictions are relaxed when going to coarser grids, the latter remains the same on all grid levels, effectively preventing the use of large time steps on coarse grids and severely limiting the overall rate of convergence. The use of a point-implicit scheme therefore relieves any such restrictions and results in overall convergence rates similar to that achieved with the mean flow equations.

At steady state the turbulence equations do not necessarily exhibit a unique solution. In regions where the production term $\mu_t P$ vanishes, $k = 0$, $\varepsilon = 0$ is an obvious solution which can be found by inspection of equations (10) and (13). However, the eddy viscosity, which is given by equation (15), becomes a ratio of two vanishing quantities and is thus undefined. The time-dependent turbulence equations, however, are not ill-posed. On the contrary, the value of the constant C_2 has been carefully chosen to ensure that k, ε and μ_t all vanish asymptotically for an isotropic decaying turbulence. For an isotropic turbulence all spatial terms as well as the production term vanish and equations (10) and (13) reduce to

$$\mathrm{d}k/\mathrm{d}t = -\varepsilon, \qquad \mathrm{d}\varepsilon/\mathrm{d}t = -C_2\frac{\varepsilon^2}{k}. \tag{24}$$

Solution of this system yields the asymptotic behaviour

$$k \approx t^{-1/(C_2-1)}, \qquad \varepsilon \approx t^{-C_2/(C_2-1)}, \qquad k^2/\varepsilon \approx t^{(C_2-2)/(C_2-1)}, \qquad t \to \infty, \tag{25}$$

which for the current value of $1 < C_2 < 2$ indicates that all quantities vanish for large t. Hence, in order to converge to the appropriate steady state solution, it is important for any numerical scheme to respect the relative asymptotic time behaviour of k and ε throughout the convergence process. For the base grid solver this is achieved by employing the maximum time step for the

system of two turbulence equations which ensures stability and positivity; letting k or ε become negative or taking too large time steps and subsequently limiting the updated values of k or ε invariably leads to unrealistic values of μ_t in the far field. Within the multigrid strategy, corrections interpolated back from the coarser grids may cause k or ε to become negative. Rather than limit these corrections, they are simply omitted at any point where positivity cannot otherwise be guaranteed. In this manner the (pointwise) time consistency is not violated and the overall effect is simply to lag such points by the effective coarse grid time step. An alternative approach would be to recompute the coarse grid corrections employing a smaller time step which guarantees positivity. However, owing to the recursive nature of multigrid, this represents a non-trivial task.

7. BOUNDARY AND INITIAL CONDITIONS

The derivation of the above turbulence transport equations is made under the hypothesis of a large-Reynolds-number flow. Thus in regions close to the wall, such as in the viscous sublayer where molecular effects become important, these equations are not valid. In order to avoid integrating the turbulence equations in these regions, we make use of wall functions. In this approach the governing equations for the flow and the turbulence are integrated up to a distance $y = y_n$ away from the wall. The flow in the remaining region $0 < y < y_n$ is assumed to obey the law of the wall, i.e.

$$\frac{U}{U_\tau} = \frac{1}{\kappa} \ln\left(\frac{\rho U_\tau y}{\mu}\right) + 5{\cdot}5. \tag{26}$$

At each time step in the solution procedure of the governing equations an estimate of the velocity U at $y = y_n$ is obtained. From this, the value of the wall shear stress can be obtained by solving equation (26) implicitly for U_τ (using a Newton–Raphson method). This estimate of the wall shear stress is then employed as a boundary condition on the momentum equation for the mean flow and results in Dirichlet wall boundary conditions for k and ε. In practice the point $y = y_n$ is very close to the wall, so that it may be approximately placed on the wall and the boundary conditions at $y = y_n$ may be imposed at the wall surface. For the momentum equation this results in a wall slip velocity $U = U(y_n)$.

In the far field k and ε are assigned freestream values at inflow boundaries and simple extrapolation is employed at outflow boundaries. Initial conditions on k and ε are obtained by imposing a level of freestream turbulence from which k is determined and ε is evaluated from equation (15) in order to produce a low value of freestream eddy viscosity ($\mu_t < 1$). However, since the present formulation results in a small value of μ_t in all regions of the flow field where production is negligible, the converged solution is relatively insensitive to the initial values of k and ε. The mean flow equations are initialized using uniform freestream flow conditions and applying the tangential slip velocity boundary condition (as for an inviscid flow). Throughout the integration process the wall shear stress obtained from equation (26), which is fed back into the momentum equation, retards the flow near the wall, thus creating a boundary layer profile.

8. RESULTS USING WALL FUNCTIONS

Two attached flow cases have been computed using the multigrid implementation of the high-Reynolds-number turbulence model described above. The first case consists of transonic flow past an RAE 2822 aerofoil. The freestream Mach number is 0·729, the incidence is 2·31°

and the Reynolds number is $6{\cdot}5 \times 10^6$. This case (case 6) has been well documented both experimentally[14] and computationally[7,13,15] on structured and unstructured meshes. The mesh employed for this case is depicted in Figure 1. It contains 12,823 vertices and exhibits a normal spacing of 10^{-4} chords at the aerofoil surface, which positions the first point off the wall in the logarithmic law-of-the-wall region. The computed Mach contours for this case are shown in Figure 2, while the resulting eddy viscosity distribution is given in Figure 3. A smooth distribution of eddy viscosity throughout the boundary layer and wake regions and vanishingly small values in the inviscid regions of flow are observed. The computed surface pressure distribution is compared with experimental data[14] in Figure 4, showing good overall agreement. The convergence rate of the system of equations is depicted in Figure 5 by plotting the RMS average of the density residual and the residual of ρk throughout the flow field versus the number of multigrid cycles. As can be seen, the flow equations and turbulence equations converge with the same asymptotic rates. The residuals are reduced by roughly six orders of magnitude over 200 cycles, yielding an overall convergence rate of 0·93.

The second case involves flow over a high-lifting four-element aerofoil. This case is useful in demonstrating the complex geometries and resulting flow fields which can be handled by the present methodology. The mesh employed is depicted in Figure 6. It contains a total of 51,100 vertices and a normal spacing of 2×10^{-4} chords off the wall for each aerofoil element. The computed Mach contours are shown in Figure 7, while the resulting eddy viscosity distribution is given in Figure 8. The ease with which multiple wakes and confluent boundary layers may be handled by the present approach is evident from the figures. The computed surface pressure distribution is seen to compare favourably with experimental wind-tunnel data[16] in Figure 9. It should, however, be pointed out that such favourable agreement is in large part due to the

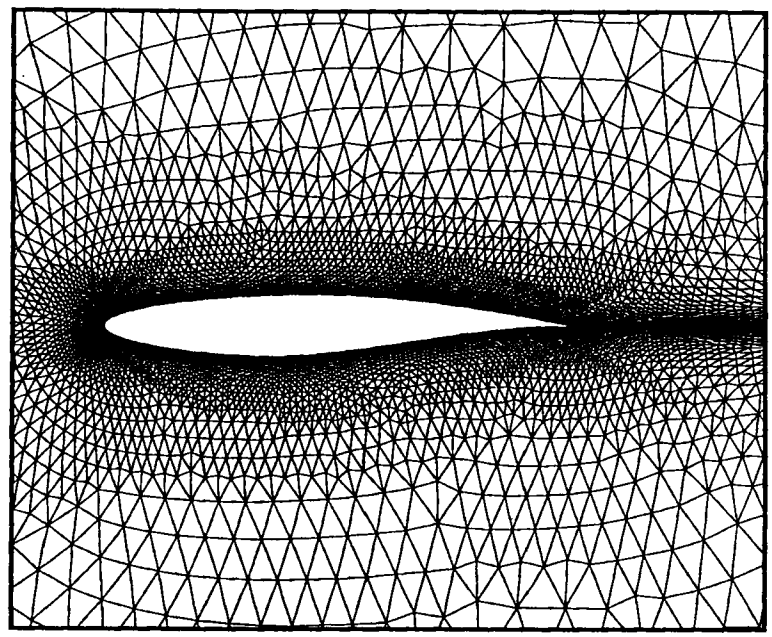

Figure 1. Unstructured mesh employed for computing flow over an RAE 2822 aerofoil (number of vertices, 12,823)

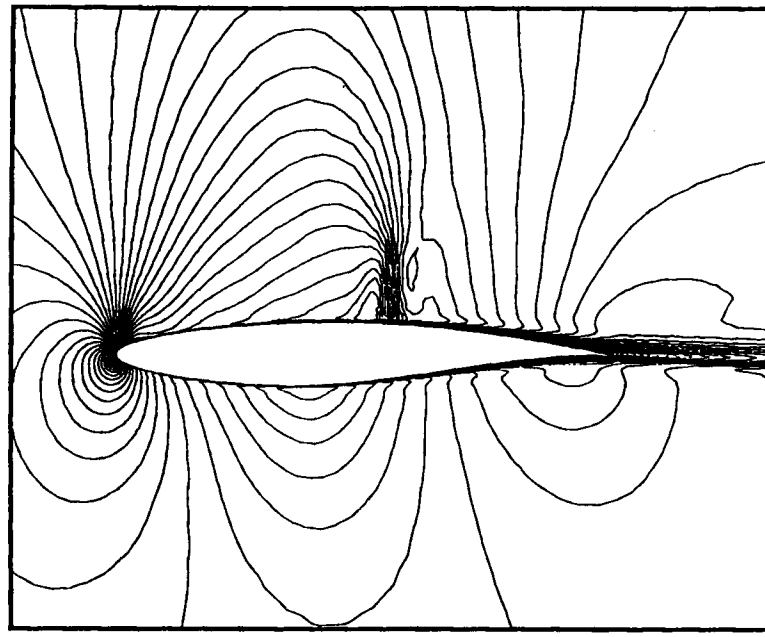

Figure 2. Computed Mach contours for turbulent flow over an RAE 2822 aerofoil using wall functions (Mach 0·729, $Re = 6{\cdot}5 \times 10^6$, incidence 2·31°)

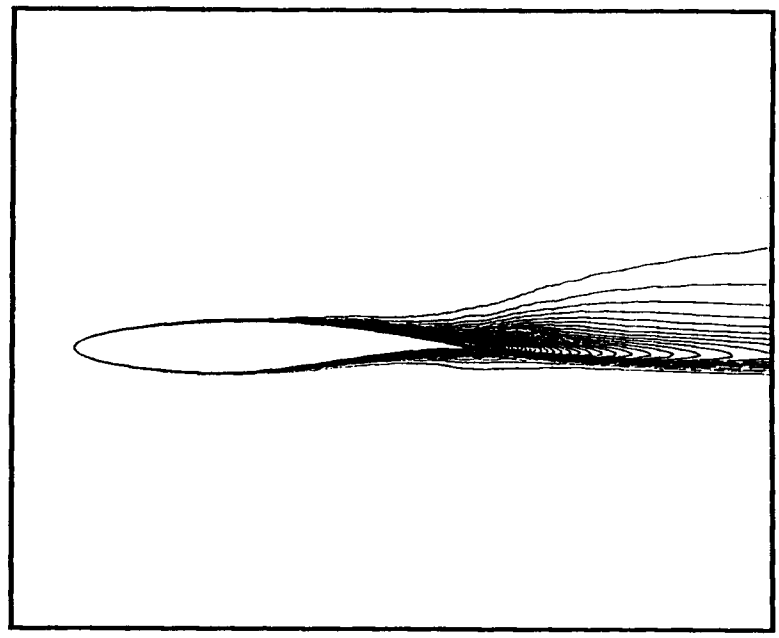

Figure 3. Computed eddy viscosity contours for turbulent flow over an RAE 2822 aerofoil using wall functions (Mach 0·729, $Re = 6{\cdot}5 \times 10^6$, incidence 2·31°)

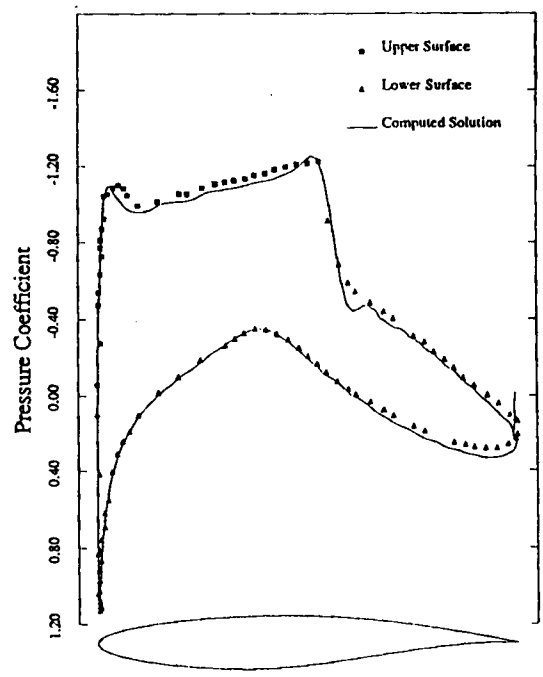

Figure 4. Comparison of computed surface pressure using wall functions with experimental measurements for flow over an RAE 2822 aerofoil (Mach 0·729, $Re = 6{\cdot}5 \times 10^6$, incidence 2·31°)

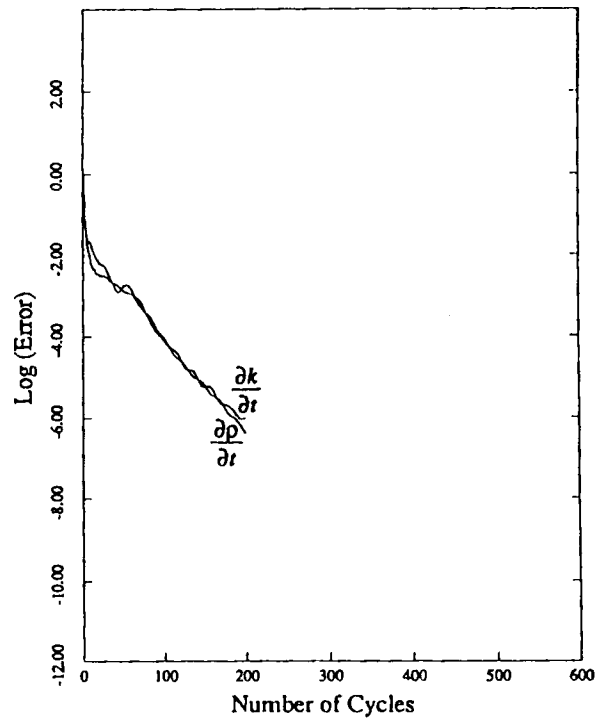

Figure 5. Convergence rate of density equation and k-equation using wall functions versus number of multigrid cycles for flow over an RAE 2822 aerofoil

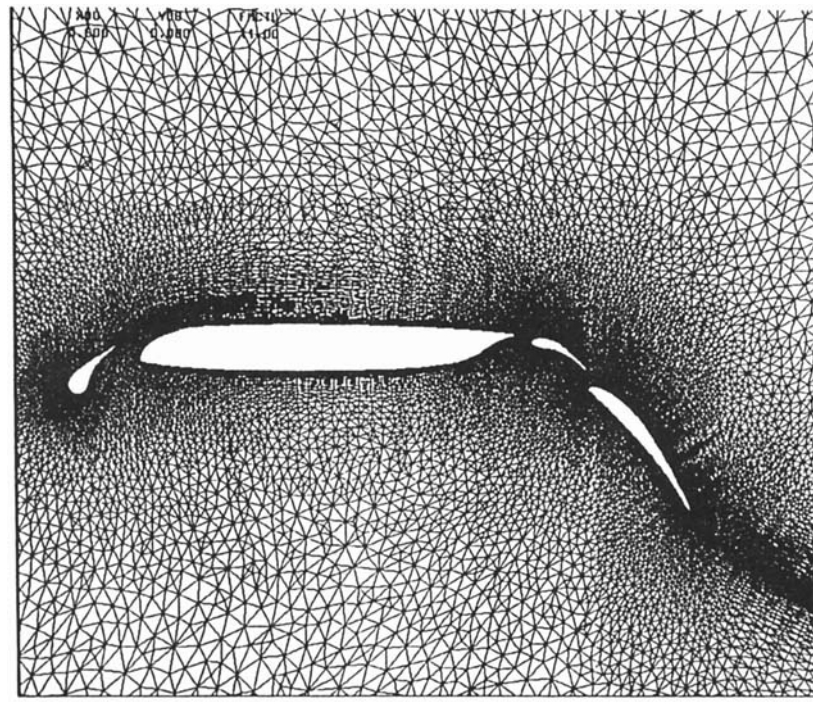

Figure 6. Unstructured mesh employed for computing flow over a four-element aerofoil (number of vertices, 51,100)

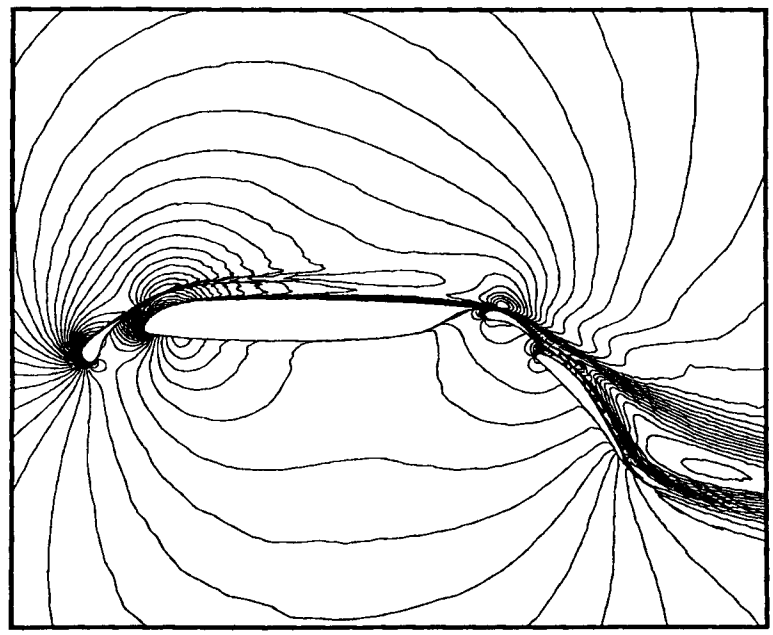

Figure 7. Computed Mach contours using wall functions for flow over a four-element aerofoil (Mach 0·2, $Re = 2{\cdot}83 \times 10^6$, incidence 8·18°)

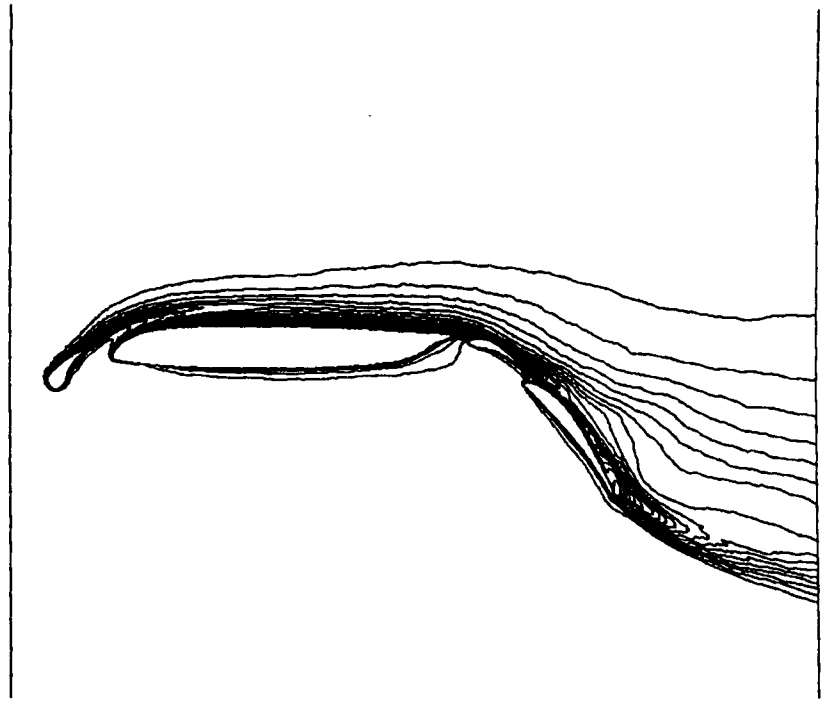

Figure 8. Computed eddy viscosity contours using wall functions for flow over a four-element aerofoil (Mach 0·2, $Re = 2{\cdot}83 \times 10^6$, incidence 8·18°)

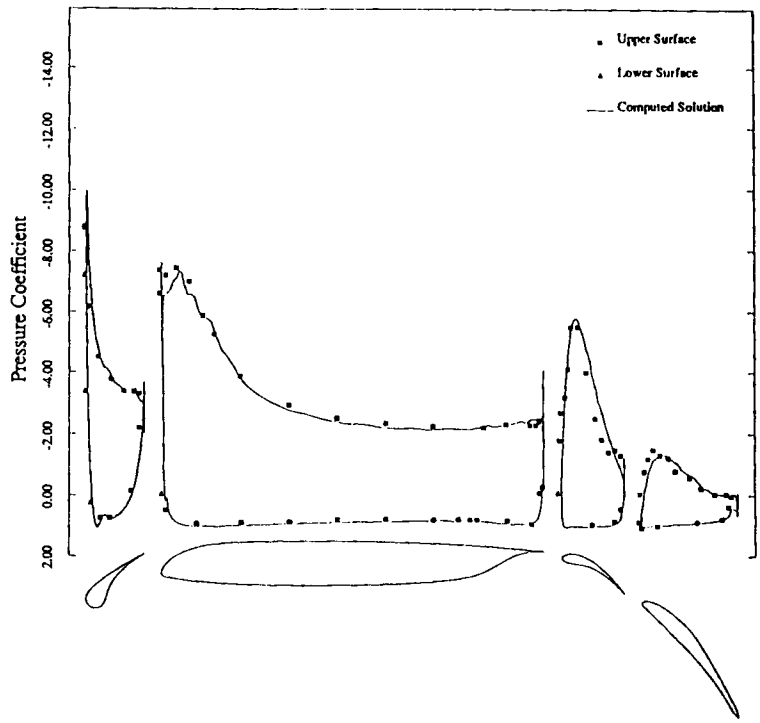

Figure 9. Comparison of computed surface pressure using wall functions with experimental wind-tunnel data for flow over a four-element aerofoil (Mach 0·2, $Re = 2{\cdot}83 \times 10^6$, incidence 8·18°)

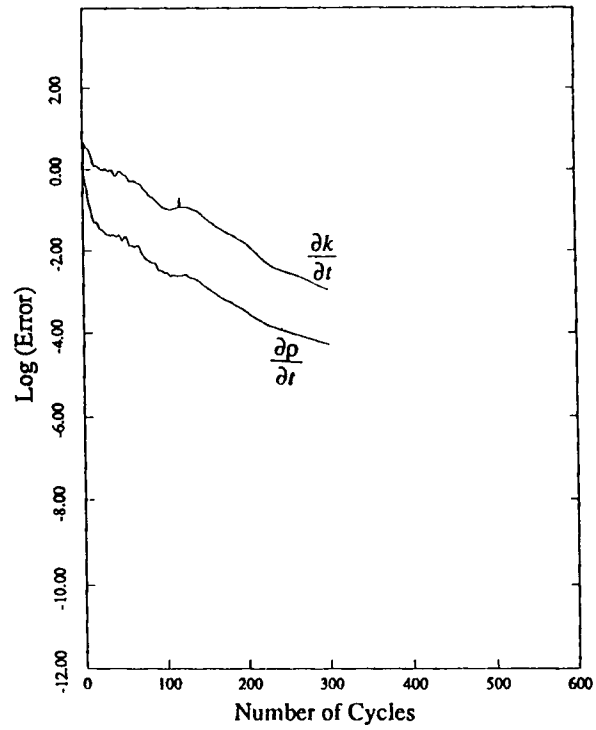

Figure 10. Multigrid convergence rate of density equation and k-equation using wall functions for flow over a four-element aerofoil

attached nature of the flow. The multigrid convergence rates of the density equation and the k-equation are depicted in Figure 10, where both equations are seen to achieve approximately the same asymptotic rates, decreasing by four orders of magnitude over 300 cycles.

9. LOW-REYNOLDS-NUMBER TURBULENCE MODEL MODIFICATIONS

While the use of the high-Reynolds-number turbulence equations in conjunction with wall functions is useful for a large class of wall-bounded flows, it is nevertheless limited to flows where a logarithmic law-of-the-wall region exists and is thus strictly not valid for separated flows. An alternative approach is to modify the turbulence equations in order to account for low-Reynolds-number effects. Many such modifications have been proposed over the years with varying degrees of success.[17] One common feature of all such modifications is that they have proved exceedingly difficult to integrate numerically very close to the wall. The aim of the present work is to develop an efficient and robust technique for integrating such models rather than reformulating or advocating any one model in particular. With this in mind we chose to implement the simplest possible low-Reynolds-number model that has been demonstrated to produce good results for simple problems, with possible extensions to more complex models should the original version prove inadequate for more complicated flows. To this end the modifications proposed by Speziale *et al.*[18] have been implemented. The modified turbulence equations, now given in vector form, can be written as

$$\frac{\partial \rho k}{\partial t} + u \cdot \nabla(\rho k) = \nabla \cdot \left[\left(\mu + \frac{\mu_t}{s_k} \right) \nabla k \right] + \mu_t P - \tfrac{2}{3} S \rho k - \rho \varepsilon,$$

$$\frac{\partial \rho \varepsilon}{\partial t} + u \cdot \nabla(\rho \varepsilon) = \nabla \cdot \left[\left(\mu + \frac{\mu_t}{s_\varepsilon} \right) \nabla \varepsilon \right] + C_1(\mu_t P - \tfrac{2}{3} S \rho k) \frac{\varepsilon}{k} - C_2 f_2 \rho \frac{\varepsilon^2}{k}, \tag{27}$$

$$\mu_t = \frac{\rho C_\mu f_\mu k^2}{\varepsilon}, \qquad f_\mu = \left(1 + \frac{3{\cdot}45}{\sqrt{Re_t}} \right) \tanh\left(\frac{-y^+}{70} \right), \qquad f_2 = \left[1 - \exp\left(\frac{-y^+}{4{\cdot}9} \right) \right]^2,$$

with boundary conditions at the wall given by

$$k = 0, \qquad \varepsilon = \frac{\mu}{\rho} \frac{\partial^2 k}{\partial y^2}, \tag{28}$$

and employing the following values for the constants:

$$C_\mu = 0{\cdot}09, \qquad \sigma_k = 1{\cdot}36, \qquad \sigma_\varepsilon = 1{\cdot}36,$$

$$C_1 = 1{\cdot}44, \qquad C_2 = 1{\cdot}83[1 - \tfrac{2}{9} \exp(-Re_t/6)^2],$$

where $Re_t = \rho k^2/\mu\varepsilon$ is the turbulence Reynolds number. As can be seen, no extra source terms are introduced and only two damping functions are required. This model is similar in form to the Lam–Bremhorst model,[19] with the notable difference that all damping functions depend solely on y^+. The evaluation of such functions requires the knowledge of the distance of each point from the closest wall. In the context of unstructured meshes this information can be constructed through the use of a generalized distance function as outlined by Barth.[20] As with most low-Reynolds-number turbulence models, the current form of the model has been reported to be extremely stiff in near-wall regions, generally requiring the prescription of initial profiles in k and ε in order to guarantee convergence to steady state. Such techniques are considered impractical for complex aerodynamic flows and thus a more robust solution strategy has been pursued. The difficulties associated with the near-wall regions can be assessed by inspection of equations (27). When the wall boundary condition $k = 0$ is substituted into the ε-equation, it is seen to result in a singularity, since k appears in the denominator of this equation. Since f_2 also vanishes at the wall, this singularity is in principle removable. However, the numerical integration of the ε-equation in its present form will only be well behaved if f_2 and k have the same asymptotic behaviour near the wall throughout the integration procedure, hence the need for start-up profiles. The approach taken in this work is to remove the singularity by solving for a new variable defined as

$$k = \tilde{k} f_2 \quad \text{or} \quad \tilde{k} = k/f_2. \tag{29}$$

Upon substituting this expression into equation (27) and using the chain rule to evaluate the gradient operators, one obtains the new set of equations

$$\begin{aligned} \frac{\partial \rho \tilde{k}}{\partial t} + u \cdot \nabla(\rho \tilde{k}) = {} & \nabla \cdot \left[\left(\mu + \frac{\mu_t}{s_k} \right) \nabla \tilde{k} \right] + \frac{1}{f_2} (\mu_t P - \tfrac{2}{3} S \rho \tilde{k} f_2 - \rho \varepsilon) \\ & + \frac{1}{f_2} \left\{ \left[\nabla \left(\mu + \frac{\mu_t}{s_k} \right) - \rho u \right] \cdot \nabla f_2 + \left(\mu + \frac{\mu_t}{s_k} \right) \nabla^2 f_2 \right\} \tilde{k} \\ & + \frac{1}{f_2} \left[2 \left(\mu + \frac{\mu_t}{s_k} \right) \nabla f_2 \cdot \nabla \tilde{k} \right], \end{aligned} \tag{30}$$

$$\frac{\partial \rho\varepsilon}{\partial t} + u \cdot \nabla(\rho\varepsilon) = \nabla \cdot \left[\left(\mu + \frac{\mu_t}{s_\varepsilon} \right) \nabla\varepsilon \right] + C_1 \frac{\mu_t P}{f_2} \frac{\varepsilon}{\tilde{k}} - \tfrac{2}{3} C_1 S \rho\varepsilon - C_2 \rho \frac{\varepsilon^2}{\tilde{k}}.$$

While the $\tilde{k}$-equation now looks rather complicated, the new terms are only significant in the region $f_2 \ll 1$, and in fact, although all terms have been included, only the term $\tilde{k}\nabla^2 f_2$ has been found to have a significant effect on the overall solution. At the wall we have

$$f_2 = 0, \qquad \nabla f_2 = 0, \qquad \nabla^2 f_2 > 0$$

as well as

$$\mu_t = 0, \qquad P = 0, \qquad S = 0, \qquad u = 0.$$

The boundary condition $k = 0$ implies $\tilde{k}$ bounded at the wall. Since f_2 which appears as a denominator on the right-hand side of the $\tilde{k}$-equation vanishes, we require the non-vanishing terms in the numerator to sum to zero, thus yielding the condition

$$\tilde{k} = \rho\varepsilon/\mu\nabla^2 f_2. \tag{31}$$

Upon substituting this expression into the ε-equation with $u = 0$, $\mu_t = 0$ and $S = 0$, one obtains a modified Helmoltz equation for ε at the wall in the steady state:

$$\nabla\mu\nabla\varepsilon - C_2 \mu \nabla^2 f_2 \varepsilon = 0. \tag{32}$$

This equation is well behaved and simple to integrate numerically. The boundary condition employed for ε is taken to be

$$\partial\varepsilon/\partial y = 0. \tag{33}$$

While it is realized that this condition may not be entirely accurate at the wall,[21] it is used at this initial stage for simplicity and may be modified in further work.

In regions removed from the wall the ε-equation remains well behaved. The k-equation on the other hand contains the source term $\tilde{k}\nabla^2 f_2$. $\nabla^2 f_2$, which can be approximated as $\mathrm{d}^2 f_2/\mathrm{d}y^2$, has the properties

$$\begin{aligned} &\nabla^2 f_2 > 0, \quad y^+ < 3{\cdot}4, \\ &\nabla^2 f_2 < 0, \quad y^+ > 3{\cdot}4, \end{aligned} \tag{34}$$

where $y^+ = 3{\cdot}4$ represents the point of inflection in the f_2-function. In regions where $\nabla^2 f_2$ is negative or zero, the k-equation is well behaved. However, $\nabla^2 f_2$ large and positive represents a growing source term, which can be numerically unstable. However, since the point $y^+ = 3{\cdot}4$ is very close to the wall and within the laminar sublayer, k can be approximated by the relation

$$k^+ = \text{constant} \times y^{+2} \tag{35}$$

or

$$\tilde{k} = \tilde{k}_{\text{wall}} y^{+2}/[1 - \exp(-y^+/4{\cdot}9)]^2, \tag{36}$$

which from direct simulations[22] is generally known to be valid up to $y^+ = 10$. Finally, in regions far away from the wall the damping functions become unity, their derivatives all vanish and the original high-Reynolds-number equations are recovered, albeit with the new values of the constants advocated in Reference 18. Thus in summary the ε-equation given in the form (30) is

employed throughout the entire flow field, except at the wall where the form (32) is used. For the $\tilde{k}$-equation the form given by equation (30) is employed from the far field up to $y^+ = 3{\cdot}4$, which is within the laminar sublayer. Below this value of y^+ equation (36) is employed with the boundary condition for $\tilde{k}$ given by equation (31).

The multigrid strategy previously described for the high-Reynolds-number turbulence equations carries over in a straightforward manner. The linearization of the source terms is now taken as

$$\frac{\partial H}{\partial w} = \begin{bmatrix} -\frac{2}{3}S + \left(\mu + \dfrac{\mu_t}{s_k}\right)\dfrac{\nabla^2 f_2}{\rho f_2} & -\dfrac{1}{f_2} \\ C_1 C_\mu f_\mu f_2 P + C_2 \dfrac{\varepsilon^2}{\tilde{k}^2} & -\frac{2}{3}C_1 S - 2C_2 \dfrac{\varepsilon}{k} \end{bmatrix}, \tag{37}$$

where the production term in the ε-equation has been simplified by the definition of μ_t in equations (27) in order to remove k from the denominator. The damping functions are evaluated only on the finest grid and interpolated up to the coarser grids, thus affording a more consistent representation of the equations on all grid levels. A full multigrid strategy is employed in which grid sequencing is used to provide an initial solution for the fine grid. In general it has been found advantageous to use the high-Reynolds-number model with wall functions on coarse grids and the low-Reynolds-number model on the finest grid when grid sequencing, thus rapidly setting up appropriate levels of eddy viscosity on the finest grid.

10. RESULTS

The present implementation of the low-Reynolds-number turbulence model has been employed to compute the turbulent boundary layer over a flat plate, the transonic flow over an RAE 2822 aerofoil and the transonic flow over a two-element aerofoil.

The mesh employed to compute the flat plate boundary layer case is depicted in Figure 11. It contains 24 points ahead of the plate, 48 points along the plate in the streamwise direction and 80 points in the direction normal to the plate. The freestream Mach number is 0·3 and the Reynolds number of the flow, based on the length of the plate, is 10^7. The first point normal to the plate is located at a distance of 2×10^{-6} plate lengths, which lies in the region $y^+ < 1$. The resulting velocity profiles are plotted in Figures 12 and 13, both in physical co-ordinates and in logarithmic wall co-ordinates, and compared with the well-known one-seventh-power-law distribution and logarithmic law-of-the-wall profile. The computed skin friction is plotted in Figure 14 versus the experimental data taken from Reference 23. The resulting distributions of k and ε are shown in Figures 15 and 16. The well-known peaks of k and ε are observed and a non-zero value of ε at the wall is obtained. These distributions are, however, slightly different from those obtained previously with the same model,[18] which may be attributed either to the different boundary condition or to the near-wall grid resolution. The overall flow quantities are nevertheless well predicted, as shown in Figures 12–14.

The transonic flow case over the RAE 2822 aerofoil presented in the previous section has been recomputed with the low-Reynolds-number turbulence model (Mach 0·729, incidence 2·31°, $Re = 6{\cdot}5 \times 10^6$). The mesh employed is similar to that shown in Figure 1, except that the normal spacing at the wall is now reduced to 1×10^{-5} chords, which results in the first mesh point off the wall in the region $1 < y^+ < 3$ over the entire surface of the aerofoil. The computed Mach contours and eddy viscosity contours are similar to those depicted in Figures 2 and 3, except

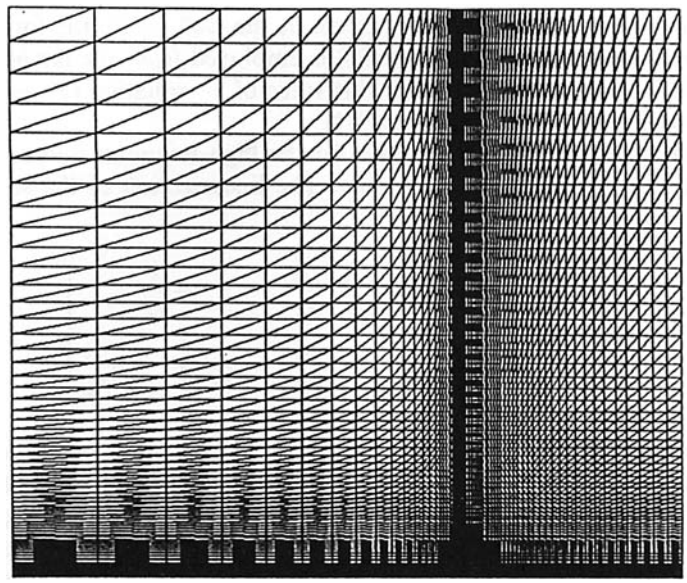

Figure 11. Triangular mesh employed for flat plate boundary layer calculation (number of vertices, 5913; 10:1 magnification in y-direction)

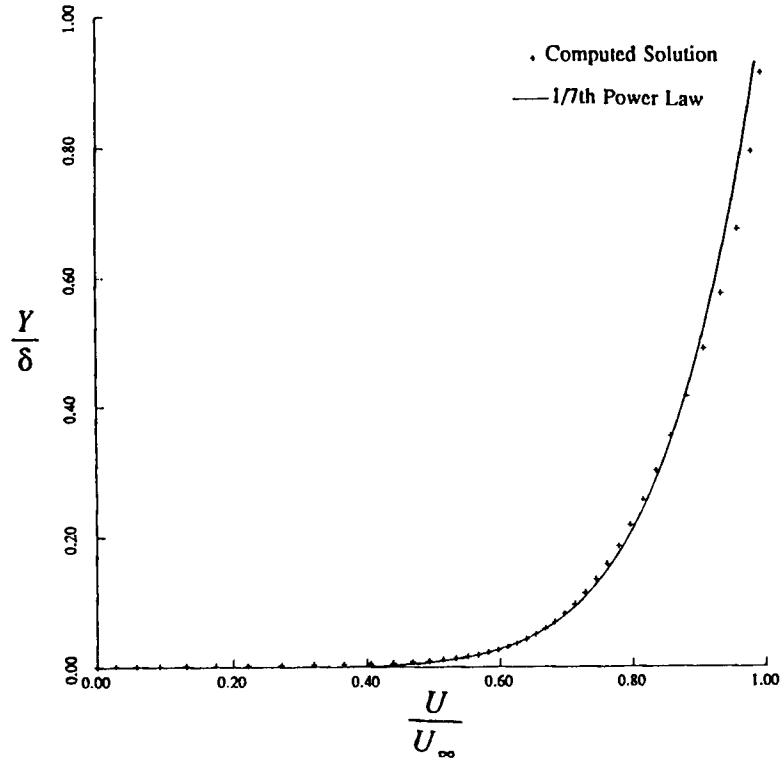

Figure 12. Computed velocity profile in physical co-ordinates versus one-seventh-power-law profile (Mach 0·3, $Re_x = 5{\cdot}3 \times 10^6$)

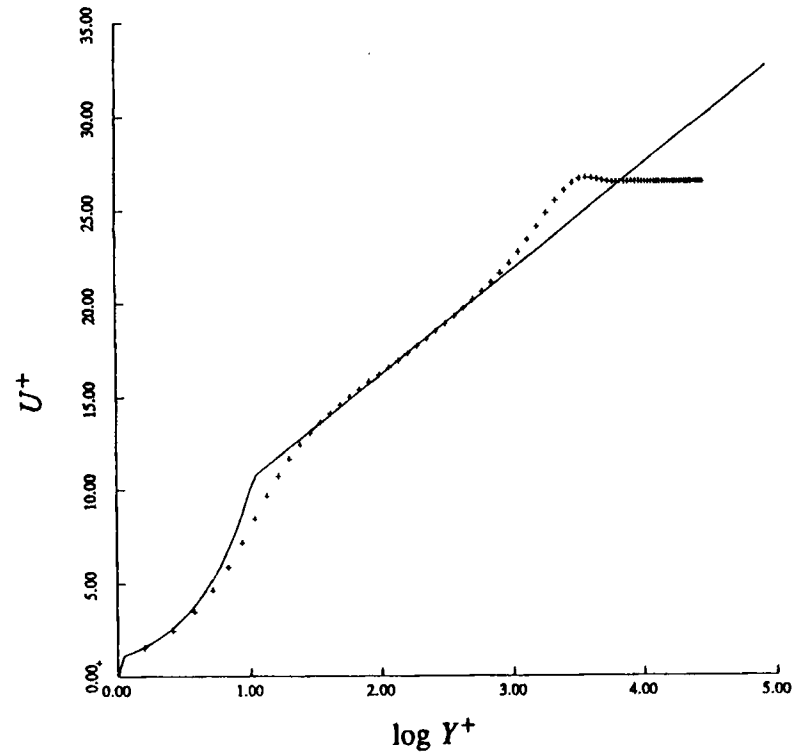

Figure 13. Computed velocity profile in logarithmic co-ordinates versus logarithmic law of the wall (Mach 0·3, $Re_x = 5{\cdot}3 \times 10^6$)

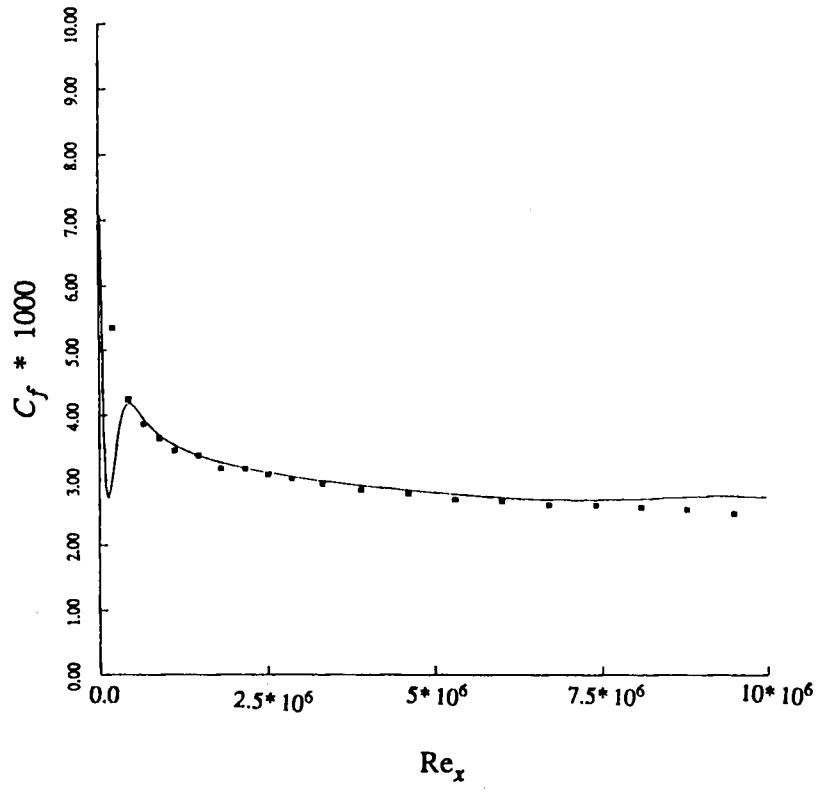

Figure 14. Computed skin friction distribution for flat plate boundary layer versus experimental data from Reference 23

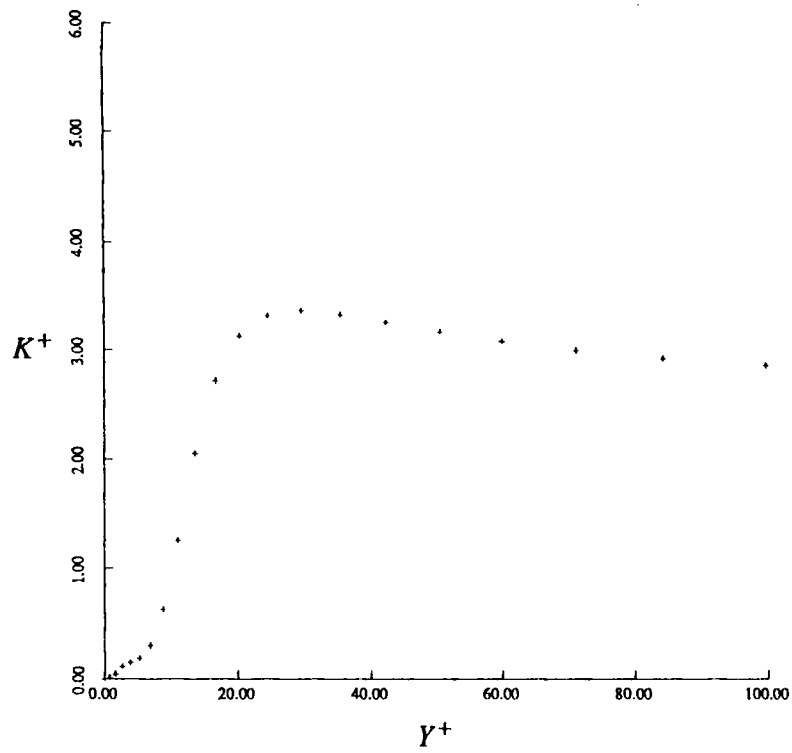

Figure 15. Computed near-wall distribution of k^+ for flat plate boundary layer (Mach 0·3, $Re_x = 5{\cdot}3 \times 10^6$)

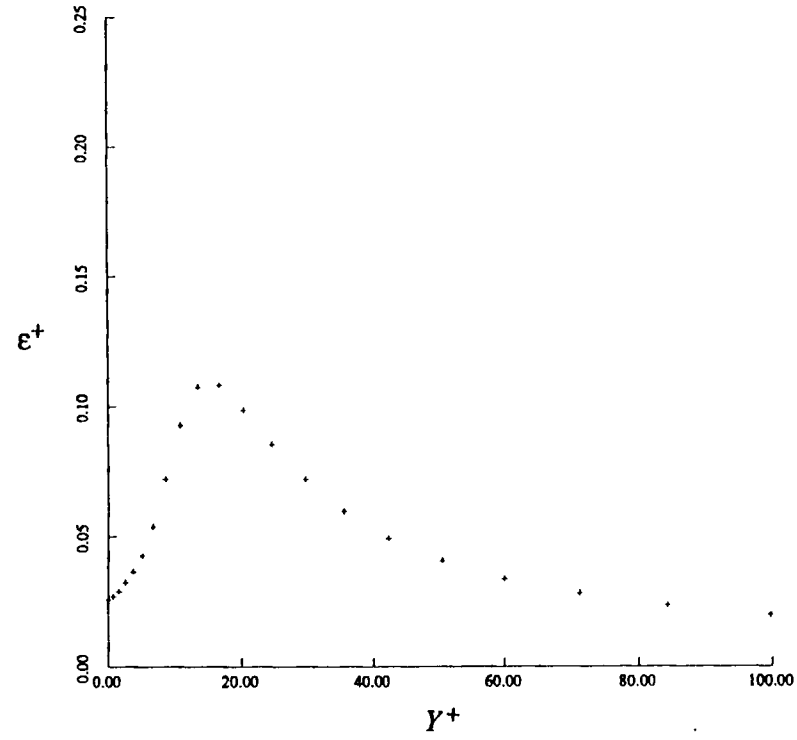

Figure 16. Computed near-wall distribution of ε^+ for flat plate boundary layer (Mach 0·3, $Re_x = 5{\cdot}3 \times 10^6$)

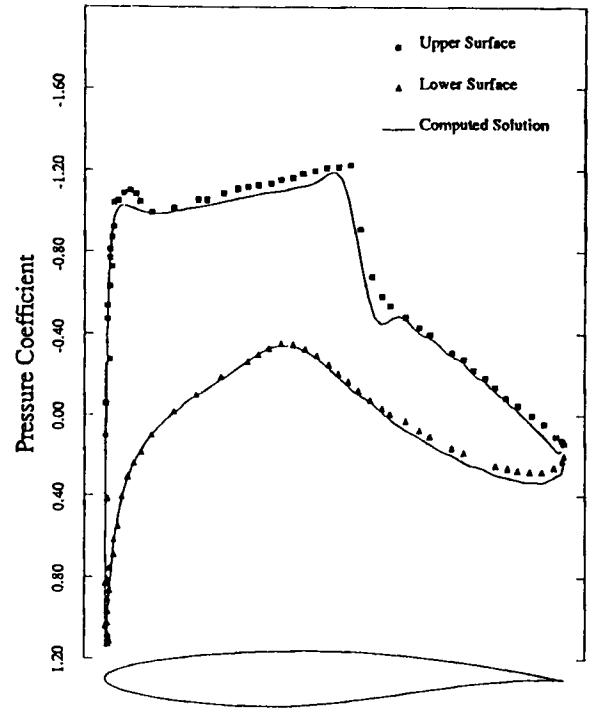

Figure 17. Computed surface pressure distribution using low-Reynolds-number modification for turbulence equations versus experimental data for flow past an RAE 2822 aerofoil (Mach 0·729, $Re = 6{\cdot}5 \times 10^6$, incidence 2·31°)

in the near-wall regions where both quantities vanish rapidly. The computed surface pressure and skin friction distributions are compared with experimental data in Figures 17 and 18. The computed lift is slightly lower than that predicted with the wall functions and that previously obtained using an algebraic model.[7] At present it is not clear whether this is due to the actual model formulation or is associated with the present implementation (artificial dissipation, grid resolution). However, the differences are rather small and the skin friction appears to be well predicted. The convergence of the density equation and the two turbulence equations is depicted in Figure 19, where the residuals are plotted versus the number of multigrid cycles on the finest grid. The flow field and turbulence equations are all initialized with uniform freestream values and 25 cycles were performed on the previous coarser grid using wall functions prior to initializing the solution procedure on the finest grid. Initializing the calculation with freestream values for all equations on the finest grid has also been employed with little degradation in convergence. From Figure 19 all equations are seen to converge at approximately the same rate, resulting in a residual reduction of four to five orders of magnitude over 300 multigrid cycles.

The final case involves the transonic flow over a two-element aerofoil. This case illustrates the ease with which complex geometries and flows with multiple viscous layers may be handled by the present methodology. The mesh employed is depicted in Figure 20. It contains a total of 28,871 vertices, with a normal spacing of 2×10^{-5} chords off the wall for each aerofoil element. The freestream Mach number is 0·5, the incidence is 7·5° and the Reynolds number is $4{\cdot}5 \times 10^6$. The computed Mach contours and eddy viscosity contours are depicted in Figures 21 and 22. Under these conditions the flow is supercritical and a shock is formed on the upper surface of

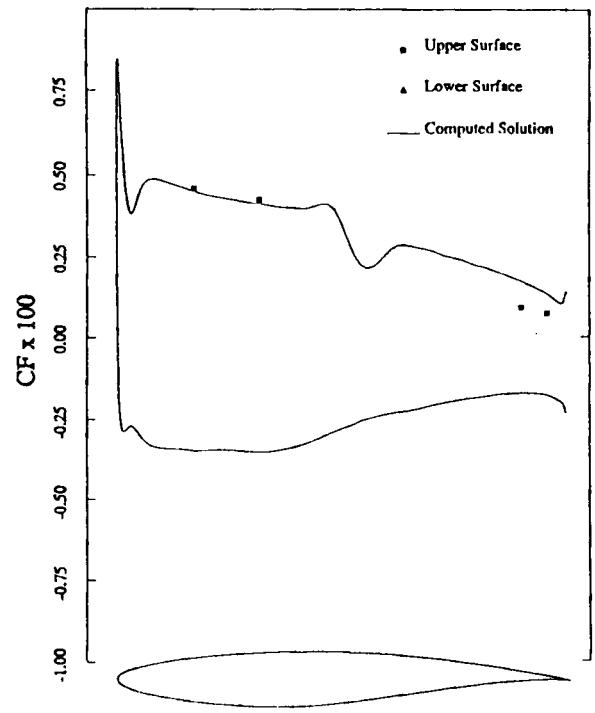

Figure 18. Computed skin friction distribution using low-Reynolds-number modification for turbulence equations versus experimental data for flow past an RAE 2822 aerofoil (Mach 0·729, $Re = 6{\cdot}5 \times 10^6$, incidence 2·31°)

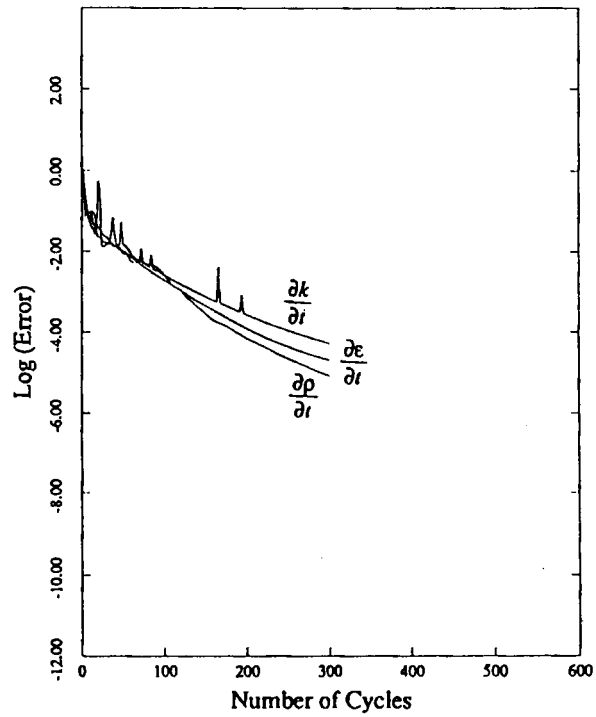

Figure 19. Convergence rate of density equation and the two turbulence equations modified for low-Reynolds-number effects versus number of multigrid cycles for flow past an RAE 2822 aerofoil

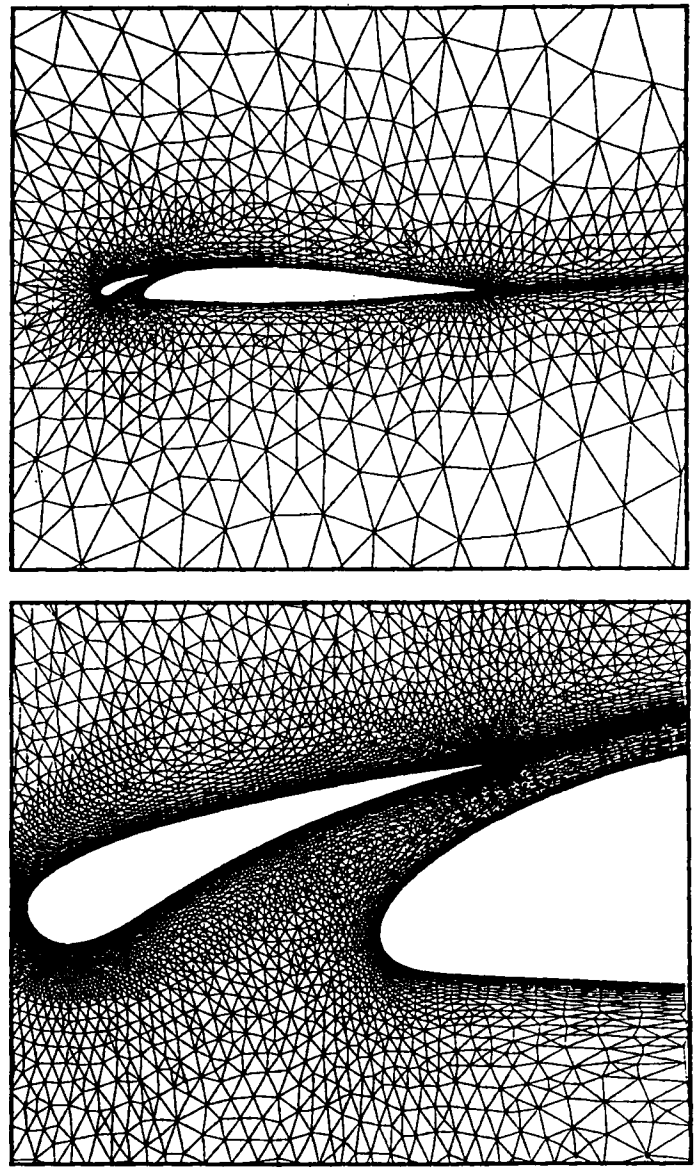

Figure 20. Global view of coarse unstructured mesh and close-up view of fine unstructured mesh employed for computing flow past a two-element aerofoil (coarse mesh points 7272, fine mesh points 28,871)

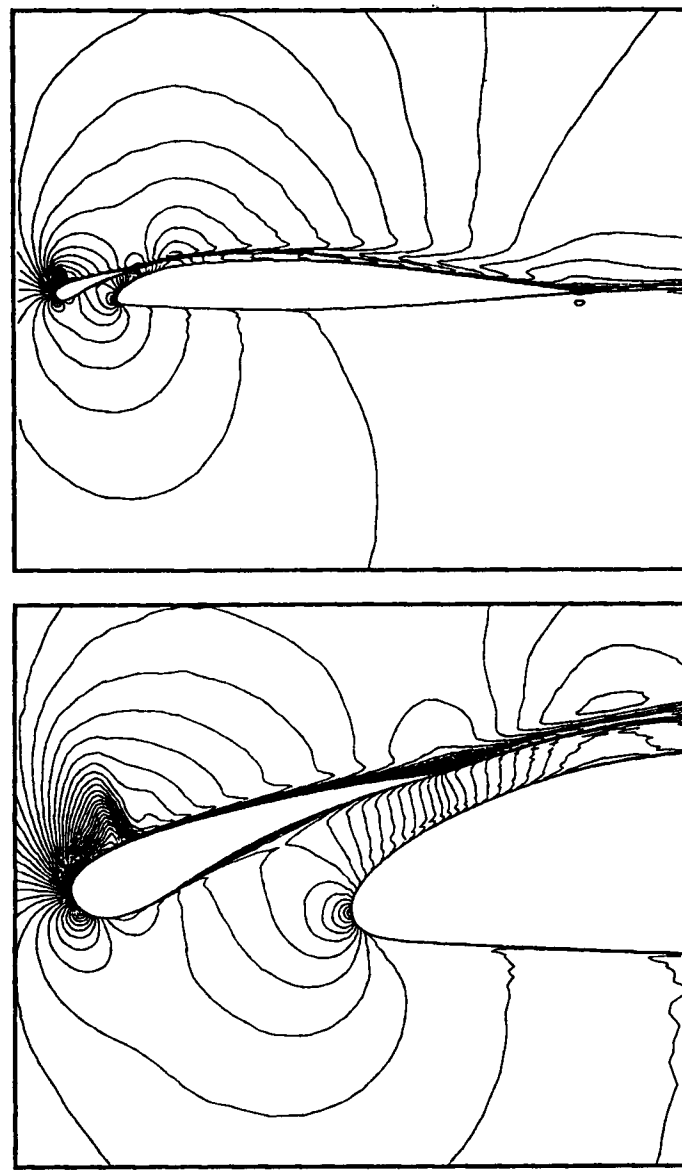

Figure 21. Computed Mach contours using low-Reynolds-number modification for turbulence equations for supercritical flow over a two-element aerofoil (Mach 0·5, $Re = 4{\cdot}5 \times 10^6$, incidence 7·5°)

the slat. A small region of separated flow occurs behind the shock, as can be seen from the skin friction plot of Figure 23. This region of separation has previously been reported in calculations using an algebraic turbulence model.[7] The computed surface pressure distribution is seen to compare favourably with experimental wind-tunnel data[24] in Figure 24. The convergence rate for this case is depicted in Figure 25, where the residuals of the density equation and the two turbulence equations are reduced by approximately three to four orders of magnitude over 300 cycles on the finest grid.

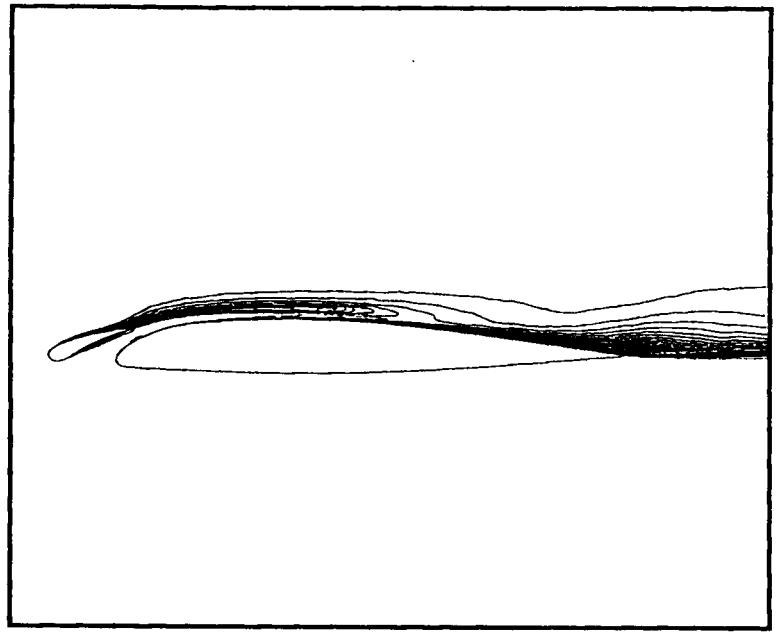

Figure 22. Computed eddy viscosity contours using low-Reynolds-number modification for turbulence equations for supercritical flow over a two-element aerofoil (Mach 0·5, $Re = 4{\cdot}5 \times 10^6$, incidence 7·5°)

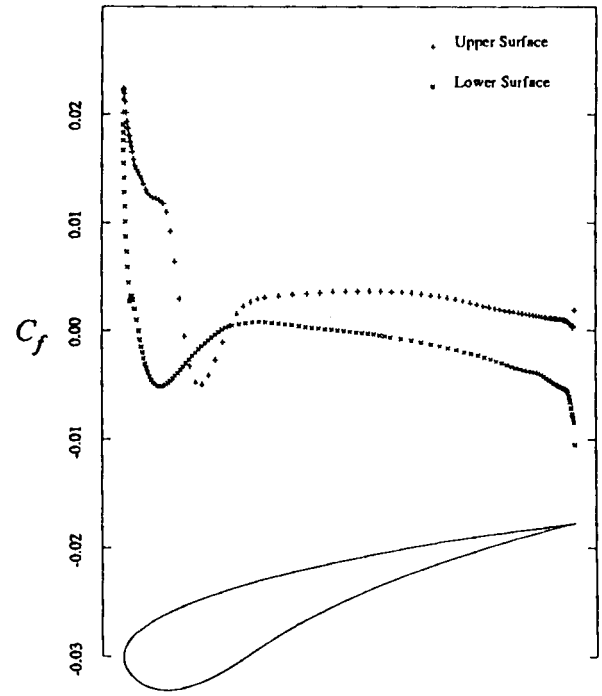

Figure 23. Computed skin friction distribution on slat showing region of separated flow behind upper surface shock (Mach 0·5, $Re = 4{\cdot}5 \times 10^6$, incidence 7·5°)

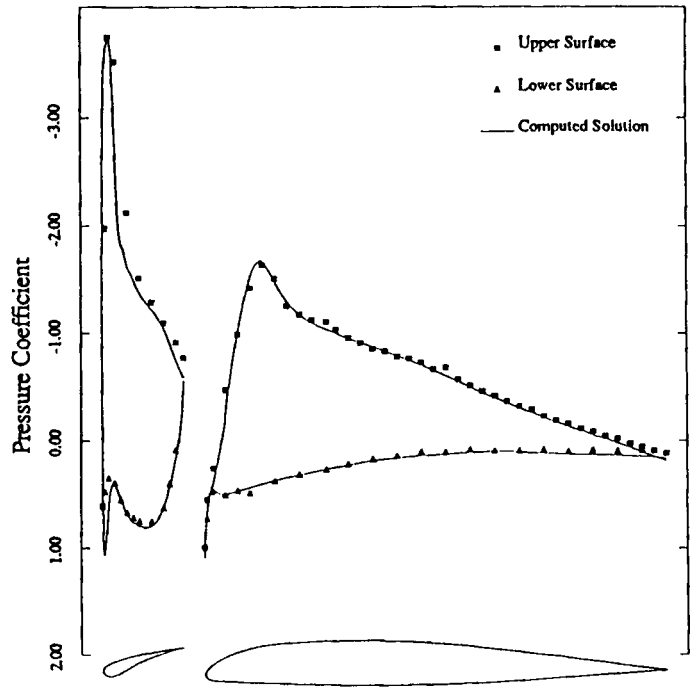

Figure 24. Computed surface pressure distribution using low-Reynolds-number modification for turbulence equations for supercritical flow over a two-element aerofoil versus experimental wind-tunnel data (Mach 0·5, $Re = 4{\cdot}5 \times 10^6$, incidence 7·5°)

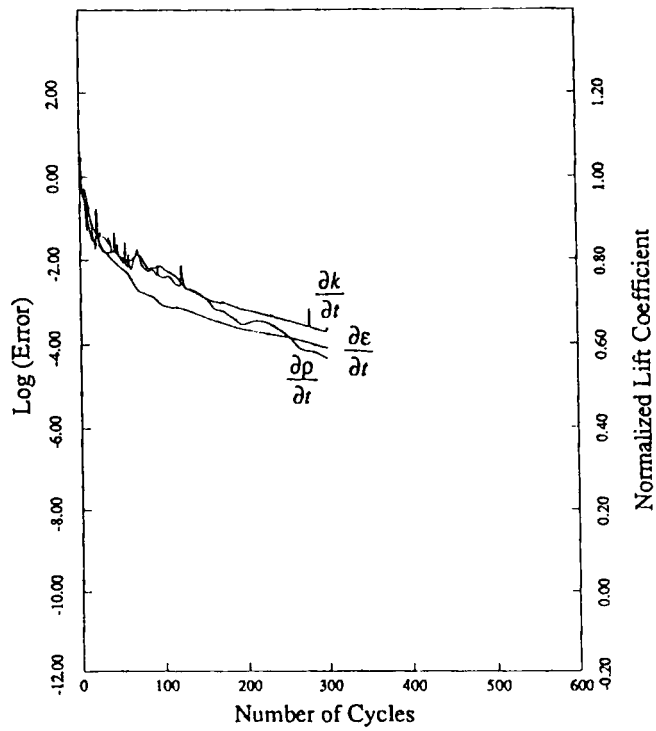

Figure 25. Multigrid convergence rate of density equation and the two turbulence equations using low-Reynolds-number modifications for flow over a two-element aerofoil (Mach 0·5, $Re = 4{\cdot}5 \times 10^6$, incidence 7·5°)

11. CONCLUSIONS

A multigrid strategy for solving the steady state, high- and low-Reynolds-number $k-\varepsilon$ turbulence equations has been formulated and implemented on unstructured meshes. A variety of aerodynamic flows have been computed, consistently demonstrating similar convergence rates for the turbulence and flow equations. Initialization of all flow and turbulence quantities may be performed using uniform freestream values. At present the evaluation of the turbulence terms requires a significant fraction of the overall time within a single time step. For example, the RAE 2822 supercritical aerofoil flow case with the low-Reynolds-number turbulence model requires roughly 2·5 s per multigrid cycle on a single processor of the Cray-YMP supercomputer, which is almost 75% higher than that required by the algebraic model reported previously.[7] However, it is estimated that this can be substantially reduced by assembling the turbulence and flow residuals simultaneously within a single loop. Given the demonstrated convergence rates, the two-equation turbulence model should be competitive in terms of computer resources with algebraic models, while providing much greater flexibility in dealing with complex geometries and flow fields.

Future work should involve a more thorough investigation of the various two-equation turbulence models and their ability in predicting complex aerodynamic flows, including flows with massive separation.

ACKNOWLEDGEMENT

This research was supported by the National Aeronautics and Space Administration under NASA Contract No. NAS1-18605 while the first author was in residence at the Institute for Computer Applications in Science and Engineering (ICASE), NASA Langley Research Center, Hampton, VA 23665, U.S.A.

REFERENCES

1. K. Morgan, J. Peraire, R. R. Thareja and J. R. Stewart, 'An adaptive finite-element scheme for the Euler and Navier–Stokes equations', *AIAA Paper 87-1172*, 1987.
2. N. P. Weatherill, L. J. Johnston, A. J. Peace and J. A. Shaw, 'A method for the solution of the Reynolds-averaged Navier–Stokes equations on triangular grids', *Proc. 7th GAMM Conf. on Numerical Methods in Fluids, Notes on Numerical Fluid Mechanics*, Vol 20, Viewey, Braunschweig, 1988.
3. N. Nakahashi, 'FDM–FEM zonal approach for viscous flow computations over multiple bodies', *AIAA Paper 87-0604*, 1987.
4. D. J. Mavriplis and A. Jameson, 'Multigrid solution of the Navier–Stokes equations on triangular meshes', *AIAA J.*, **28**, 1415–1425 (1990).
5. D. G. Holmes and S. D. Connell, 'Solution of the 2D Navier–Stokes equations on unstructured adaptive grids', *AIAA Paper 89-1932*, 1989.
6. B. S. Baldwin and H. Lomax, 'Thin layer approximation and algebraic model for separated turbulent flows', *AIAA Paper 78-275*, 1978.
7. D. J. Mavriplis, 'Algebraic turbulence modeling for unstructured and adaptive meshes', *AIAA Paper 90-1653*, 1990.
8. K. P. Dimitriadis and M. A. Leschziner, 'Multilevel convergence acceleration for viscous and turbulent transonic flows computed with a cell-vertex method', in J. Mandel, S. McCormick, J. Dendy, G. Lonsdale, S. Parter, J. Ruge and K. Stuben (eds), *Proc. Fourth Copper Mountain Conf. on Multigrid Methods*, Copper Mountain, CO, April 1989, SIAM, Philadelphia, PA, 1989, pp. 130–148.
9. G. A. Gerolymos, 'Implicit multiple-grid solution of the compressible Navier–Stokes equations using $k-\varepsilon$ turbulence closure', *AIAA J.*, **28**, 1707–1717 (1990).
10. D. J. Mavriplis, 'Multigrid solution of the two-dimensional Euler equations on unstructured triangular meshes', *AIAA J.*, **26**, 824–831 (1988).
11. B. E. Launder and D. B. Spalding, 'The numerical computation of turbulent flows', *Comput. Methods Appl. Mech. Eng.*, **3**, 269–289 (1974).
12. L. Martinelli, 'Calculations of viscous flows with a multgrid method', *Ph.D. Thesis*, Department of Mechanical and Aerospace Engineering, Princeton University, 1987.

13. L. Martinelli and A. Jameson, 'Validation of a multigrid method for the Reynolds averaged equations', *AIAA Paper 88-0414*, 1988.
14. P. H. Cook, M. A. McDonald and M. C. P. Firmin, 'Aerofoil RAE 2822 pressure distributions and boundary layer and wake measurements', *AGARD Advisory Rep. 138*, 1979.
15. T. J. Coakley, 'Numerical simulation of viscous transonic airfoil flows', *AIAA Paper 87-0416*, 1987.
16. E. Omar, T. Zierten, M. Hahn, E. Szpizo and A. Mahal, 'Two-dimensional wind-tunnel tests of a NASA supercritical airfoil with various high-lift systems, Volume II—Test data', *NASA CR 2215*, 1977.
17. V. C. Patel, W. Rodi and G. Scheuerer, 'Turbulence models for near-wall and low Reynolds number flows: a review', *AIAA J.*, **23**, 1308–1319 (1985).
18. C. G. Speziale, R. Abid and E. C. Anderson, 'A critical evaluation of two-equation models for near wall turbulence', *ICASE Rep. 90-46*, *NASA CR 182068*, *AIAA Paper 90-1481*, 1990.
19. C. K. G. Lam and K. Bremhorst, 'A modified form of the k–ε model for predicting wall turbulence', *J. Fluids Eng.*, **103**, 456–460 (1981).
20. T. J. Barth, 'Numerical aspects of computing viscous high-Reynolds number flows on unstructured meshes', *AIAA Paper 91-0721*, 1991.
21. N. N. Mansour, J. Kim and P. Moin, 'Reynolds stress and dissipation rate budgets in turbulent channel flow', *J. Fluid Mech.*, **194**, 15–44 (1988).
22. J. Kim, P. Moin and R. Moser, 'Turbulence statistics in fully developed channel flow at low Reynolds number', *J. Fluid Mech.*, **177**, 133–166 (1987).
23. K. Wieghardt and W. Tillmann, 'On the turbulent friction layer for rising pressure', *NACA TM 1314*, 1951.
24. G. Volpe, 'A multigrid method for computing the transonic flow over two closely-coupled airfoil components', *ICAS Paper 84-1.4.3*, 1984.